Sustainable Energy & Fuels

ROYAL SOCIETY OF CHEMISTRY

PAPER

View Article Online
View Journal | View Issue

Cite this: *Sustainable Energy Fuels*, 2025, **9**, 5236

Production of jet-fuel precursors from volatile fatty acids using metal oxide-supported zeolitic catalysts

Adrián Lago,[abc] Lorenzo Bertin,[de] Gonzalo A. Martinez,[d] Emma Jones,[d] Jacopo De Maron,[fg] Tommaso Tabanelli,[fg] Fabrizio Cavani,[fg] Cristina González-Fernández,[bhi] David P. Serrano[ac] and Inés Moreno *[ac]

This study investigates the vapor-phase ketonization of hexanoic acid (HA) to produce 6-undecanone (6-UN), a key intermediate for sustainable aviation fuels (SAF), using bifunctional catalysts composed of metal oxides supported on acidic zeolites. A screening of metal oxides (TiO_2, ZrO_2, CeO_2) supported on H-ZSM-5 identified TiO_2 as the most active phase. Although HA conversion decreased over time on stream (TOS), 6-UN selectivity increased up to 90%, due to the deactivation of Brønsted acid sites (BAS) that minimizes side reactions like cracking and aromatization. In contrast, Lewis acid sites (LAS), essential for ketonization, remained more stable. The effect of supporting TiO_2 on different zeolites (H-ZSM-5, H-β, and USY) was also evaluated. TiO_2/H-β showed the highest 6-UN yield due to its high LAS concentration and large mesoporous surface area (271 m^2 g^{-1}), highlighting the importance of acidity and textural properties. TiO_2/H-β also demonstrated strong stability when tested with crude bio-HA derived from grape pomace fermentation. Additionally, Na-exchanged H-ZSM-5 confirmed that removing BAS improved ketonization performance, though not as effectively as TiO_2/H-β, reinforcing the latter's superior catalytic behavior.

Received 2nd July 2025
Accepted 13th August 2025

DOI: 10.1039/d5se00930h

rsc.li/sustainable-energy

1. Introduction

Aviation is one of the most energy-intensive sectors and has been the fastest-growing mode of transport in recent years, with an estimated contribution of 4% to the EU's total greenhouse gas (GHG) emissions.[1,2] To address this issue, the European Commission has proposed a mandate for the blending of Sustainable Aviation Fuels (SAF) – renewable or waste-derived fuels – requiring a gradual increase in the minimum share of SAF from 2% in 2025 to 70% by 2050 (based on energy content).[1,3] This new regulatory framework will require the development of innovative manufacturing processes for SAF to meet the projected demand of up to 28.6 million tonnes by that date.[1,4] The Hydroprocessed Esters and Fatty Acids (HEFA) process, which relies on vegetable oils and waste fats, is currently the only commercial route for SAF production. However, this pathway cannot meet the future demand due to feedstock limitations and competition with other biofuels production.[5,6] Various technologies have emerged in recent years, such as biomass gasification combined with Fischer–Tropsch (Gas + FT), Alcohols-to-Jet (AtJ), and Power-to-Liquids (PtL). Nevertheless, these processes face significant challenges, including high costs, low efficiencies, and limited technology readiness levels.[7–9]

Anaerobic digestion (AD) is a widely used technology for converting organic wastes[10] into biogas (and nutrient rich digestate), with its industrial application expanding rapidly. Interestingly, the AD process can be easily transformed into an open mixed culture anaerobic fermentation (MCAF) by increasing the organic loading rate and tuning other operating parameters such as residence time, pH, and temperature. This allows to produce an effluent rich in C_2–C_6 volatile fatty acids (VFAs),[11] which are considered platform molecules for the production of biofuels or biobased products.[5]

To meet the key operational property specifications such as freezing point, viscosity, and flash point, jet fuels must be composed predominantly of linear alkanes with a carbon chain

[a]*Thermochemical Processes Unit, IMDEA Energy, Avda. Ramón de la Sagra 3, 28935, Móstoles, Madrid, Spain*
[b]*Biotechnology Processes Unit, IMDEA Energy, Avda. Ramón de la Sagra 3, 28935, Móstoles, Madrid, Spain*
[c]*Chemical and Environmental Engineering Group, ESCET, Rey Juan Carlos University, 28933, Móstoles, Madrid, Spain. E-mail: ines.moreno@imdea.org*
[d]*Department of Civil, Chemical, Environmental and Materials Engineering (DICAM), University of Bologna, Via Terracini 28, 40131 Bologna, Italy*
[e]*Department of Food and Drug Sciences, University of Parma, Parco Area delle Scienze 27/A, 43124 Parma, Italy*
[f]*Department of Industrial Chemistry "Toso Montanari", University of Bologna, Viale del Risorgimento 4, Bologna, 40136, Italy*
[g]*Center for Chemical Catalysis-C3, University of Bologna, Viale del Risorgimento 4, Bologna, 40136, Italy*
[h]*Department of Chemical Engineering and Environmental Technology, School of Industrial Engineering, University of Valladolid, Dr Mergelina, s/n, Valladolid, 47011, Spain*
[i]*Institute of Sustainable Processes, Dr Mergelina, s/n, Valladolid, 47011, Spain*

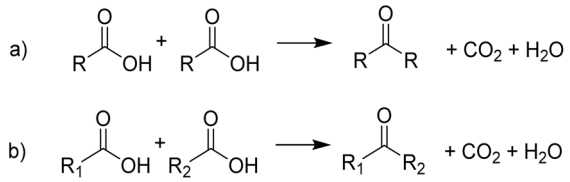

Scheme 1 Carboxylic acids (a) homo-ketonization or (b) cross-ketonization.

length between 8 and 15 carbon atoms, centered around C_{11}.[12] In this context, C^{4+} VFAs can be converted into the corresponding *n*-alkanes *via* ketonization followed by a hydrodeoxygenation (HDO).[5] Ketonization, or ketonic decarboxylation, is a carbon–carbon coupling catalytic reaction in which two carboxylic acid molecules react to form a single ketone molecule, producing CO_2 and water as by-products (Scheme 1).

This process has been extensively studied for short-chain fatty acids such as acetic acid[13,14] and propionic acid[15–17] which are relatively abundant in pyrolysis bio-oils, yielding C_3 and C_5 ketones, respectively. However, these carbon chain lengths are insufficient to meet SAF specifications and require an additional step, such as aldol condensation.[5] This issue can be overcome by using longer-chain VFAs, such as the hexanoic acid (HA), which leads to the formation of a C_{11} ketone that can be directly hydrodeoxygenated into the corresponding C_{11} *n*-alkane. Despite the significant potential held by this route and the growing interest in its application to SAF production, studies involving the ketonization of medium chain-length VFAs, particularly HA, are surprisingly limited.[18,19] Moreover, the available literature focuses exclusively to the use of pure commercial reagents, thus neglecting the challenges posed by the low VFAs concentration in aqueous fermented streams and the potential impact of impurities on catalyst performance and stability. In this context, Martinez *et al.* recently succeeded in producing HA at a high concentration through the acidogenic chain elongation fermentation of the ethanol contained in grape pomace. The strength of this process lies in the straightforward subsequent purification method that involves the acidification of the fermentation broth to trigger the separation of an organic phase containing approximately 90 wt% HA,[20] which has been used to produce biopolymers,[20] diesel blendstocks[21] and flavors and fragrances.[22]

Metal oxides, such as TiO_2,[23,24] ZrO_2,[12,25,26] and CeO_2,[15,27] have been investigated as ketonization catalysts due to their high stability and selectivity toward ketones. Their catalytic performance is attributed to the presence of Lewis acid sites (LAS), which promote the α-H elimination from one carboxylic acid molecule and the C–C coupling *via* a β-keto acid intermediate.[16,28] However, the catalytic activity of these materials is limited by their low specific surface area (4–126 $m^2\ g^{-1}$).[29–31]

Ketonization of VFAs over zeolites has also been reported in the literature.[28,32] However, zeolites lead to a broader product distribution (including aromatics, olefins, *etc.*) than metal oxides due to the promotion of a number of side reactions, such as aldol condensation, cracking, cyclization, aromatization, among others, catalyzed by the Brønsted acid sites (BAS) of the zeolite.[18,33,34] Consequently, mild conditions have to be employed to achieve a significant ketone selectivity, which in turn limits VFAs conversion.[35] In addition, zeolites suffer faster deactivation than metal oxides due to the strong adsorption of carboxylic acids and the pore blockage caused by coke deposition.[36]

The deposition of metal oxides (such as Ga, Fe, Zn, Y, Ti, and others) on zeolites can modulate their catalytic activity and improve their stability by moderating the Brønsted acidity of the zeolite, being also an effective way for incorporating Lewis acid sites (LAS) from the metal oxide.[32] This strategy has been investigated for the ketonization of VFAs present in pyrolysis oils[37,38] but it has not yet been evaluated for the ketonization of longer carbon chain VFAs, such as HA, identifying a research gap in this topic.

In this context, as far as we know, this work is the first dealing with the ketonization of HA using bifunctional metal oxide-based catalysts supported on different acidic zeolites, as well as the first report on the performance of such catalytic materials in the ketonization of a real crude feedstock obtained by fermentation. Zeolitic supports are expected to provide the high surface area that metal oxides typically lack, while the metal oxides contribute to the content of LAS, effectively fine-tuning the acidic properties of the zeolite. To this end, an active phase screening was performed by testing TiO_2, ZrO_2 and CeO_2 oxides supported on a commercial H-ZSM-5 zeolite. After identifying the most active metal oxide phase, different commercial zeolites (H-β, USY and H-ZSM-5) were evaluated as supports. The best-performing bifunctional catalyst was then applied to the ketonization of real HA-rich effluent. In addition, the effect of modulating the acidity of the H-ZSM-5 *via* a Na^+ ion exchange treatment on the ketonization activity was assessed.

2. Materials and methods

2.1 Bio-hexanoic acid derived from grape pomace

The hexanoic acid was produced from red grape pomace by using the same procedure recently described.[22] Briefly, the red grape pomace was fed into a five-step countercurrent leaching process with water which allowed to obtain: (A) an ethanol solution (30–40 g L^{-1}) to be fermented for hexanoic acid production; and (B) an ethanol-exhausted grape pomace that could be further valorized (*e.g.* seed oil extraction; not the aim of this work). Thereafter, the corresponding ethanol solution was fermented in batch mode at 30 L scale (37 °C and pH 7) to obtain 22–25 g L^{-1} of bio-HA. At the end of the fermentation, the biomass was separated from the broth by centrifugation (Beckman J2-HS; 8000 rpm, 6 °C, 15 min) and the liquid fraction was acidified with commercial H_2SO_4 96% until pH level was 2. The resulting HA formed an oily upper phase that was separated from the water-phase with a separatory funnel. This crude biotechnological HA (henceforth bio-HA) was characterized in terms of its organic and inorganic composition and stock at room temperature until used. Major organic composition of the bio-HA was identified using gas chromatography-mass spectrometry (GC-MS) and quantified by gas chromatography-flame ionization detection (GC-FID). The GC-MS analysis was

performed on an Agilent Technologies 6890 system equipped with an HP-5 capillary column (30 m × 250 μm × 1.05 μm) coupled with an Agilent Technologies 5973 quadrupole mass spectrometer. The GC-FID analysis was conducted on a Hewlett Packard 5890 Series II system equipped with a flame ionization detector and an Agilent J&W DB-1701 capillary column (25 m × 530 μm × 1.05 μm). The inorganic cations contained in the bio-HA were determined *via* elemental analysis using microwave plasma atomic emission spectroscopy (MP-AES) on an Agilent 4210 instrument.

2.2 Catalyst preparation

Three commercial acidic zeolites with different structures (MFI, BEA and FAU) were used as catalytic supports: ZSM-5 zeolite (H-ZSM-5, Clariant, ref. HCZP 90, $[Si/Al]_{MOL} = 42$), β zeolite (H-β, Clariant, ref. CP 811E-75, $[Si/Al]_{MOL} = 38$) and ultrastable zeolite Y (USY, Zeolyst, ref. CBV780, $[Si/Al]_{MOL} = 40$).

Metal oxide active phases (TiO_2, ZrO_2, and CeO_2) were loaded on the zeolitic supports following a wet impregnation method. Typically, 5 g of the zeolitic support was added to a round bottom flask containing 50 mL of ethanol along with the metallic precursor ($C_{10}H_{14}O_5Ti$, Aldrich, 90 wt%, $Zr(C_5H_7O_2)_4$ Aldrich, 97 wt% or $Ce(NO_3)_3 \cdot 6H_2O$, Alfa Aesar, 99.9 wt%). The amount of these precursors was calculated to achieve a nominal metal oxide loading of 15 wt%. The resulting solution was stirred at 60 °C for 6 h, after which the solvent was eliminated using a rotary evaporator. The recovered catalyst was dried at 105 °C overnight and, finally, calcined in a static air furnace at 550 °C for 5 h.

Additionally, the H-ZSM-5 support was subjected to a Na^+ ion exchange treatment to reduce the BAS concentration.[39] Specifically, 10 g of the zeolite were added to a 100 mL of a 0.2 M Na_2CO_3 (99.9%, Sigma-Aldrich) aqueous solution. This suspension was stirred for 16 h at room temperature, filtered, and washed with distilled water. This procedure was repeated three times to ensure a complete ion exchange. The resulting catalyst, named Na-ZSM-5, was then dried overnight at 105 °C before TiO_2 deposition, following the above-described procedure.

2.3 Catalyst characterization

The zeolite crystallinity and the presence of TiO_2, ZrO_2, and CeO_2 clusters on the zeolite surface were evaluated by X-ray diffraction (XRD) analyses conducted on a Philips PW 3040/00 X'Pert MPD/MRD diffractometer using Cu Kα radiation (λ = 1.5406 Å), operated at 45 kV and 40 mA in a 2θ range of 5–90° with a step size of 0.013° and time per step of 39.525 s. The aluminum content and metal loading of the catalysts were determined by inductively coupled plasma optical emission spectroscopy (ICP-OES) using a PerkinElmer Optima 7300 DV instrument. The textural properties were estimated from Ar adsorption–desorption isotherms measured at −186 °C on a Micromeritics 3Flex instrument, after degassing the materials at 300 °C for 5 h. The surface area was determined using the BET (S_{BET}) equation, while the total pore volume (V_P) was determined at a $P/P_0 = 0.97$. Surface and volume corresponding to the zeolitic micropores (S_{MZ} and V_{MZ}) and mesoporous and external surface (S_{MS+EXT}) were calculated by applying the NL-DFT model, following the previously disclosed methodology.[40,41]

The concentrations of Brønsted and Lewis acid sites were determined by pyridine adsorption followed by FT-IR (Py-FT-IR) using a Jasco 4600 instrument equipped with a TGS detector in a home-built system.[40,42] First, a self-supported wafer (15 mg cm^{-2}) was prepared and activated under vacuum (10^{-4} mbar) at 480 °C for 1 h prior to the measurements. After cooling the sample to 150 °C, pyridine was introduced into the cell for 20 min and then vacuum treated for 30 min, before recording the FT-IR spectrum at the same temperature. Transmission electron microscopy (TEM) was employed to study the morphology of the zeolitic samples while scanning electron microscopy (SEM) was used to evaluate the dispersion of the active phase nanoparticles on the support surface. SEM micrographs were taken in a FESEM JEOL microscope operating at 1 kV in a GSBH mode and equipped with an Energy Dispersive X-ray Spectroscopy accessory, while TEM images were collected in both JEOL JEM 2100 (200 kV) and JEOL JEM 1400 (120 kV) microscopes.

Coke deposited on the spent catalysts was quantified by TG-DTA analysis, performed from room temperature to 900 °C at a heating rate of 10 °C min^{-1} under an air flow of 100 mL min^{-1} using a Netzsch STA-449-F3 instrument equipped with a SiC furnace.

2.4 Catalytic tests and products characterization

Ketonization tests were carried out in a vapor-phase atmospheric fixed-bed quartz reactor described elsewhere[25] introducing 0.5 mL of catalyst. Prior to the reaction, the catalyst sample was pelletized, crushed, and sieved to a particle size ranging from 30 to 60 mesh. Then, pure HA (Sigma-Aldrich, 99.9 wt%) or bio-HA was fed into the reactor using a KD Scientific Legacy 100 volumetric pump equipped with a 5 mL glass syringe. Nitrogen was used as the carrier gas with a substrate/gas molar ratio of 0.1 and a contact time of 0.5 s. Once the desired temperature was reached (375–400 °C), the substrate was fed into the reactor for 5 h. The reactor inlet was preheated at 220 °C to evaporate the substrate before entering the reactor. Condensable products were collected hourly in two bubblers containing acetonitrile (Sigma-Aldrich) and then analyzed offline using a Shimadzu GC-2025 equipped with a FID detector and an Agilent HP-5 capillary column (30 m × 0.32 mm ID × 0.25 μm), using nitrogen as carrier gas (2 mL min^{-1}) and dodecane as an internal standard. The reaction products were previously identified using an Agilent 6890 GC instrument coupled to an Agilent 5973 quadrupole mass analyzer (GC-MS) and an Agilent HP-5 capillary column (30 m × 0.25 mm × 1.05 μm). Non-condensable products were analyzed on-line using an Agilent 3000A micro-GC instrument equipped with 3 columns: PlotQ, OV1 and a molecular sieve 5A, using argon as carrier gas and a thermal conductivity detector (TCD).

Reaction parameters including HA conversion (X_{HA}), product selectivity (S_i) and mol C yields (Y_i) were calculated using the following equations:

$$X_{HA}\ (\%) = \frac{n^0_{HA} - n^F_{HA}}{n^0_{HA}} \times 100 \quad (1)$$

$$S_i(\%) = \frac{n_i}{n^0_{HA} - n^F_{HA}} \times 100 \quad (2)$$

$$Y_i(\%) = \frac{n_i \times nC_i}{n^0_{HA} \times nC_{HA}} \times 100 \quad (3)$$

Being n^0_{HA} the total HA amount fed into the system (mol), n^F_{HA} the amount of HA recovered at the exit of the reactor (mol), n_i the moles of each product formed in the reaction, nC_i the number of carbon atoms in the product and nC_{HA} the number of carbon atoms in HA.

3. Results and discussion

3.1 Screening of the metal oxide active phase in the ketonization of HA over H-ZSM-5 support

Different metal oxide active phases (TiO_2, ZrO_2, and CeO_2) with a nominal 15 wt% metal oxide loading supported on a commercial H-ZSM-5 zeolite were evaluated in the vapor-phase ketonization of HA. First, these catalysts were characterized to determine their main physicochemical properties. The XRD patterns (Fig. S1) indicate that, in all cases, the impregnated catalysts maintain a high crystallinity, showing the typical diffraction signals of the MFI structure (2θ = 8–10° and 20–25°).[43] However, the intensity of the MFI peaks decreases after the metal oxide loading, which is attributed to a shielding effect of the metal oxide nanoparticles when deposited on the zeolite surface. The characteristic reflections corresponding to the metal oxides can also be seen in the spectra of the supported catalysts. Thus, in the case of TiO_2/H-ZSM-5, the characteristic reflections of anatase are found at 2θ values of 25.3°, 37.8° and 55.0°, which has been reported to be the most active TiO_2 phase for VFA ketonization.[32] The signals at 2θ = 30.0°, 50.1° and 60.0° and 2θ = 28.6°, 33.1°, 47.5° and 56.4° in the diffractograms corresponding to ZrO_2/H-ZSM-5 and CeO_2/H-ZSM-5 denote the formation of tetragonal ZrO_2 and CeO_2 nanoparticles, respectively.

Table 1 summarizes the textural properties obtained from the Ar adsorption–desorption isotherms at −186 °C (see Fig. S2). As observed, the parent H-ZSM-5 support exhibits a Type I isotherm (according to the IUPAC classification), typical of microporous materials. This isotherm also exhibits strong adsorption at relative pressures higher than 0.8, denoting high interparticle adsorption due to the nanosized morphology of the zeolitic crystals of this sample, as can be observed in the TEM images depicted in Fig. S3. The deposition of the metal oxides on the H-ZSM-5 zeolite results in minimal variations in the Ar adsorption–desorption isotherms. Thus, there is a slight reduction in the hysteresis loop width and in the Ar capacity at intermediate relative pressures, indicating that the metal oxide deposition primarily occurs on the outer surface of the zeolite. Consequently, the micropore surface area of H-ZSM-5 remains largely unchanged after the incorporation of these metal oxides.

Chemical analyses, performed by ICP-OES, indicate that the metal loadings in all samples (14.9–16.8 wt%) are in the range of theoretical values (Table 1). On the other hand, Table 1 also presents the BAS and LAS concentrations, measured by means of pyridine adsorption followed by FT-IR. As observed, metal oxide loading reduces the BAS concentration due to the partial surface coverage caused by the deposition of metal oxide species. In contrast, an increase in the LAS concentration is observed, from 0.03 mmol g^{-1} to 0.09 mmol g^{-1}, 0.08 mmol g^{-1} and 0.07 mmol g^{-1} when TiO_2, ZrO_2 and CeO_2 are incorporated, respectively, denoting that the deposition of metal oxides on the zeolitic support generates additional LAS compared to the parent zeolite.

The catalytic performance of H-ZSM-5 and the different metal oxides supported samples was evaluated in terms of HA conversion, selectivity and mol C yield toward the HA ketonization target product, 6-undecanone (6-UN) (Fig. 1). The distributions of secondary products in both condensed and gas phases are depicted in Fig. S4 and S5.

Complete HA conversion (Fig. 1A) is observed in all cases at a TOS of 1 h, after which it decreases sharply, denoting significant catalyst deactivation. The best conversion results at the end of the experiments (TOS = 5 h) are obtained using TiO_2 as the active phase (X_{HA} = 42.2%) followed by ZrO_2 (X_{HA} = 34.8%) and CeO_2 (X_{HA} = 14.8%), the latter showing a lower conversion than the bare H-ZSM-5 (X_{HA} = 16.3%). The selectivity toward 6-UN (Fig. 1B) is very limited at short TOS but it gradually increases over time. Metal oxide supported catalysts achieve higher selectivity toward 6-UN at the end of the TOS ($S_{6\text{-UN}}$ of 92.1%, 81.5%, and 65.3% for ZrO_2/H-ZSM-5, TiO_2/H-ZSM-5, and CeO_2/H-ZSM-5 respectively) compared to the raw H-ZSM-5 ($S_{6\text{-UN}}$ = 39.2%). The main secondary products in the liquid phase are monoaromatic hydrocarbons (Fig. S4) such as toluene, xylenes and C_9, C_{10} and C_{11} aromatics, with mol C yields of 2.6–5.6%, 3.8–6.7%, 2.5–5.3%, 1.7–2.2% and 0.4–1.5% at TOS of 1 h,

Table 1 Textural, acid properties and metal loading of parent H-ZSM-5 and supported catalysts

Catalysts	S_{BET}[a] ($m^2\ g^{-1}$)	S_{MZ}[b] ($m^2\ g^{-1}$)	S_{EXT}[b] ($m^2\ g^{-1}$)	V_{MZ}[b] ($cm^3\ g^{-1}$)	V_T[c] ($cm^3\ g^{-1}$)	C_L[d] (mmol g^{-1})	C_B[d] (mmol g^{-1})	Metal oxide loading[e] (wt%)
H-ZSM-5	388	282	106	0.176	0.458	0.03	0.25	—
TiO_2/H-ZSM-5	337	242	95	0.151	0.417	0.09	0.19	16.8
ZrO_2/H-ZSM-5	343	255	88	0.158	0.419	0.08	0.17	15.8
CeO_2/H-ZSM-5	346	255	91	0.159	0.414	0.07	0.21	14.9

[a] BET surface area from Ar adsorption–desorption isotherms (−186 °C). [b] Calculated by applying NL-DFT method to Ar adsorption–desorption isotherms (−186 °C). [c] Measured at P/P_0 = 0.97. [d] Determined by means of pyridine adsorption followed by FT-IR. [e] Estimated from ICP-AOS analyses.

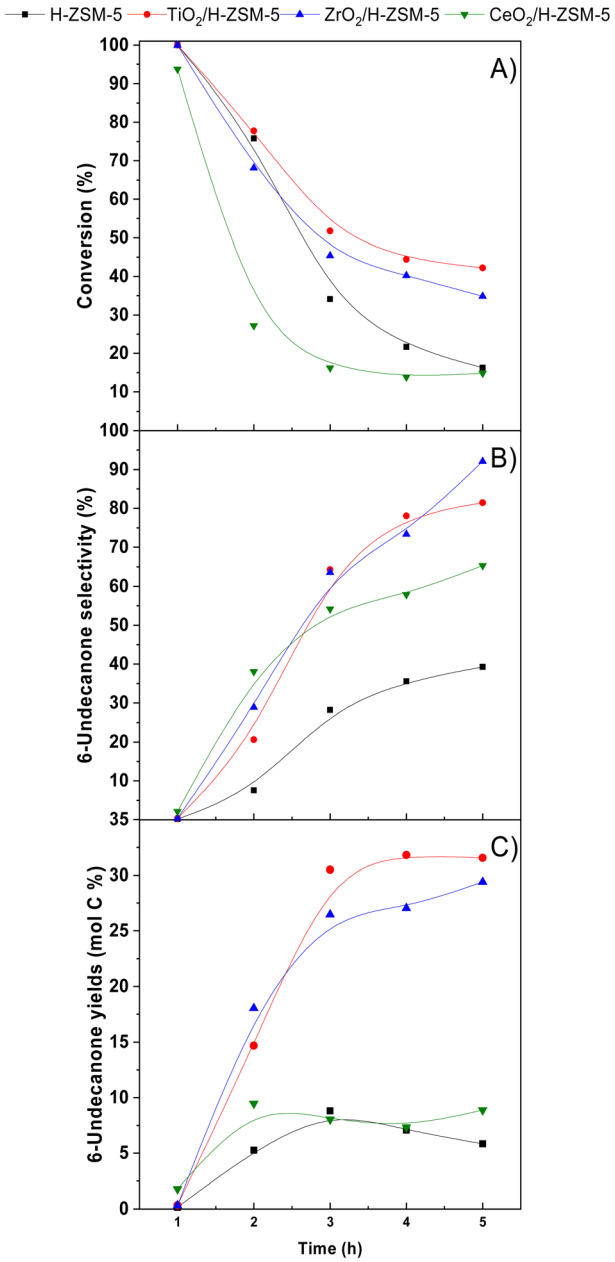

Fig. 1 HA conversion (A), 6-UN selectivity (B) and 6-UN mol C yield (C) obtained over H-ZSM-5 and metal oxide supported catalysts.

respectively. Aromatic hydrocarbons can be formed by successive reactions including deoxygenation, cyclization and aromatization of 6-UN and/or cracking and deoxygenation of both HA and ketone to form olefins, which can be further converted into aromatics through oligomerization–cyclization and aromatization (OCA) reaction sequence.[44–46] Thus, a significant amount of light olefins, mainly propylene (11.0–11.7% mol C) and some butenes (0.6–0.9% mol C) are detected in the gaseous fraction at a TOS of 1 h, as shown in Fig. S5. In this line, the CO_2 yield closely matched the value predicted by the stoichiometry of the ketonization reaction, supporting the reaction sequence proposed so far.

The wide distribution of the carbon chain lengths in these aromatic hydrocarbons also suggests the occurrence of dealkylation or transalkylation processes,[47] which can evolved into polyaromatic hydrocarbons and, finally, coke. Considering this product distribution and the information reported in the literature, Scheme 2 presents a tentative reaction scheme illustrating the conversion routes of HA over this type of bifunctional catalysts.

According to the literature, the main cause of deactivation is the strong adsorption of carboxylic acid molecules on the BAS and, to a lesser extent, the pore blockage by coke deposition,[18,32] which in these samples achieved values of 8.7–9.2 wt% at TOS of 5 h, as determined by TG analyses. This phenomenon probably explains the decrease in the formation of aromatic hydrocarbons (Fig. S4), as it is mainly catalyzed by BAS. TiO_2 and ZrO_2 supported catalysts, which have the lowest BAS density, are the most resistant materials to deactivation. Interestingly, the production of 6-UN, which is catalyzed by LAS, increases along the reaction time, especially over TiO_2 and ZrO_2 supported samples, achieving values of 31.5 mol C % and 29.4 mol C %, respectively, at a TOS of 5 h.

Over time, as the BAS deactivate, the HA and the produced 6-UN are no longer consumed for aromatics formation. This leads to an increase in both 6-UN selectivity and yield, despite the decrease in conversion, which reaches almost constant values at around a TOS of 3 h. At the end of the experiments, the catalysts with the highest 6-UN yield are TiO_2/H-ZSM-5 (31.6 mol C %) and ZrO_2/H-ZSM-5 (29.4 mol C %), followed by CeO_2/H-ZSM-5 (8.9 mol C %) and finally the parent zeolite (5.8 mol C %). Accordingly, the ketonization activity diminishes following this order: $TiO_2 > ZrO_2 > CeO_2$. TiO_2 exhibits a slightly better activity than ZrO_2, since it is able to incorporate a slightly higher amount of LAS into the catalyst.

This study demonstrates that incorporating metal oxides on zeolitic supports, particularly H-ZSM-5, enhances the ketonization activity of the parent zeolite, improving both selectivity and yield toward 6-UN as well as resistance to deactivation. Among the metal oxides tested, TiO_2 is the most efficient active phase, resulting in the highest HA conversion and selectivity and yield toward 6-UN. Therefore, TiO_2 was selected as the active phase to be supported on other zeolitic supports, (H-β and USY zeolites) to evaluate the effect of the zeolitic structure on the ketonization of HA.

3.2 Screening of the zeolitic support for the HA ketonization TiO_2 catalysts

In this section, the performance of different zeolitic materials (H-ZSM-5, H-β, and USY) as supports for the ketonization of HA using TiO_2 as the active phase was evaluated.

Wide-angle XRD analyses (Fig. S6) show that the TiO_2 impregnation does not affect the crystalline structure of the zeolitic supports, as the characteristic peaks of the MFI ($2\theta = 8$–10° and 20–25°), BEA ($2\theta = 7.7°$ and 22.3°), and FAU ($2\theta = 6.3$, 10.10 and 15.67°) topologies are retained after the metal oxide loading.[48] Nevertheless, the intensity of these signals is lower in the impregnated catalysts due to the shielding effect induced by

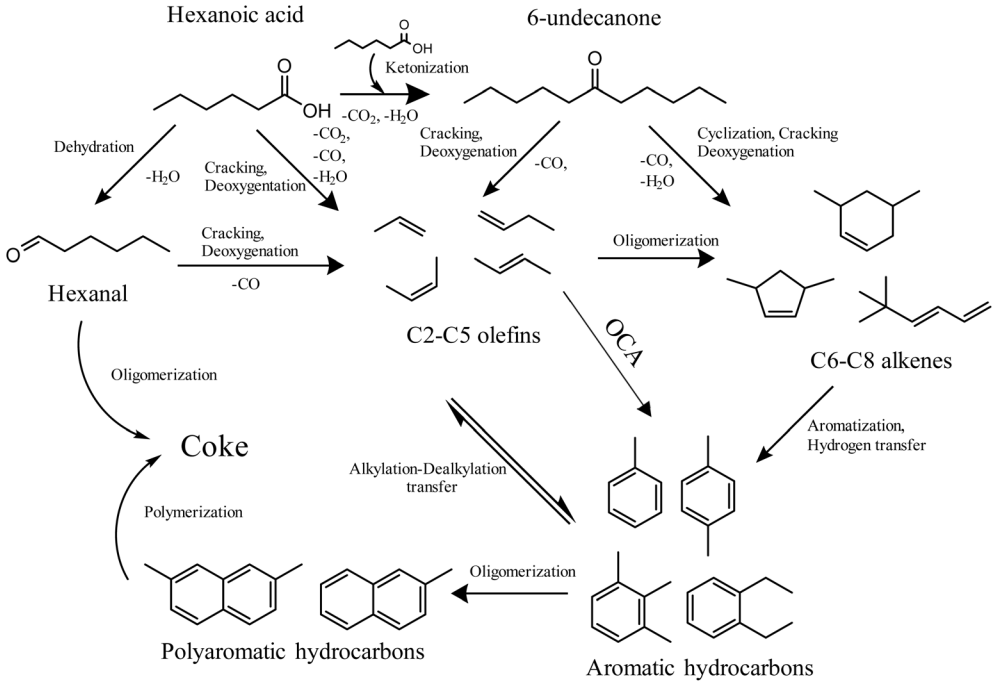

Scheme 2 Proposed reaction scheme of HA conversion over supported metal oxides over H-ZSM-5 catalysts.

the incorporation of the metal oxide phase. Furthermore, the incorporation of TiO_2 is evident through the appearance of anatase characteristic peaks at 2θ values of 25.3°, 37.8° and 55.0°.

The Ar adsorption–desorption isotherms at −186 °C of the bifunctional catalysts, as well as of the bare zeolites are presented in Fig. S7 A–C. As observed, the parent zeolites exhibit isotherms that combine characteristics of type I and IV according to the IUPAC classification. Thus, these materials are mostly microporous, as evidenced by the high adsorption that appeared at relative pressures <0.1, although the shape of the isotherms indicates the existence of some additional porosity, whose contribution to the porous structure of the material varies significantly from one zeolite to another. As discussed in the previous section, the high adsorption observed in the isotherm of H-ZSM-5 at $P/P_0 > 0.8$ is attributed to the existence of interparticular voids in addition to the intrinsic MFI microporosity. The isotherm of the H-β zeolite showed a significant Ar uptake at medium-high relative pressures, indicating the presence of a non-uniform mesopore size distribution, which is an unusual feature for commercial β zeolites. According to the TEM images (Fig. S8), the zeolitic particles of this sample are formed by aggregates of very small zeolitic nano-units with sizes around 20 nm and the additional mesopores arise from the voids existing between them. Meanwhile, the isotherm of the USY zeolite shows slight adsorption at intermediate relative pressures along with a narrow hysteresis loop ranging from P/P_0 of 0.4 to 0.95. These features suggest the presence of some mesopores, which could be formed during the stabilization process by extensive dealumination of the original Y zeolite to obtain the USY form.

The textural properties estimated from the Ar physisorption analyses are summarized in Table 2. USY zeolite exhibits the largest S_{BET} (746 $m^2\ g^{-1}$), which is mainly associated with its zeolitic micropores (S_{MZ} = 657 $m^2\ g^{-1}$), with a minor contribution from the external and mesopore surface (89 $m^2\ g^{-1}$). H-

Table 2 Physical and chemical characterization of H-ZSM-5, H-β, USY zeolite and TiO_2 supported catalysts

Catalysts	S_{BET}[a] ($m^2\ g^{-1}$)	S_{MZ}[b] ($m^2\ g^{-1}$)	S_{EXT}[b] ($m^2\ g^{-1}$)	V_{MZ}[b] ($cm^3\ g^{-1}$)	V_T[c] ($cm^3\ g^{-1}$)	C_L[d] (mmol g^{-1})	C_B[d] (mmol g^{-1})	Metal oxide loading[e] (wt%)
H-ZSM-5	388	282	106	0.176	0.458	0.03	0.25	—
TiO_2/H-ZSM-5	337	242	95	0.151	0.417	0.09	0.19	16.8
H-β	595	356	239	0.211	0.932	0.09	0.17	
TiO_2/H-β	507	343	164	0.202	0.672	0.16	0.12	16.5
USY	746	657	89	0.289	0.527	0.03	0.06	
TiO_2/USY	655	596	59	0.262	0.435	0.13	0.07	17.2

[a] BET surface area from Ar adsorption–desorption isotherms (−186 °C). [b] Calculated by applying NL-DFT method to Ar adsorption–desorption isotherms (−186 °C). [c] Measured at P/P_0 = 0.97. [d] Determined by means of pyridine adsorption followed by FT-IR. [e] Estimated from ICP-AOS analyses.

ZSM-5 presents the lowest S_{BET} (388 m^2 g^{-1}) and the smallest microporous surface (275 m^2 g^{-1}), although it has a higher contribution from the external area compared to USY zeolite due to its nanocrystalline morphology. H-β has intermediate S_{BET} and S_{MZ} values (595 and 356 m^2 g^{-1}, respectively), but it stands out for its large contribution of mesopores and external area (239 m^2 g^{-1}), which is a direct consequence of the ultra-small size of its zeolitic nanounits, as can be observed in Fig. S8.

All supported catalysts show reduced adsorption compared to the raw supports, resulting in lower textural parameters. For MFI and BEA catalysts, this decrease has a minimal impact on the surface area and volume associated with the zeolitic micropores, suggesting that the TiO_2 nanoparticles are mainly deposited in the external surface of the zeolite. In contrast, for TiO_2/USY, the active phase loading also results in a more pronounced reduction in these textural properties, denoting a partial pore blockage of the zeolitic micropores.

The Brønsted and Lewis acid site concentrations (C_B and C_L, respectively), determined by Py-FT-IR spectroscopy, are also included in Table 2. Although all zeolitic supports exhibit similar $[Si/Al]_{MOL}$ ratios (ranging from 38–42), their acidic properties differ significantly. Thus, while C_B is always higher than C_L in all zeolitic supports, the concentration of the former decreases as follows: H-ZSM-5 (0.25 mmol g^{-1}) > H-β (0.17 mmol g^{-1}) > USY (0.06 mmol g^{-1}). Likewise, the concentration of Lewis sites was 0.03 mmol g^{-1} for H-ZSM-5 and USY zeolite, which is significantly lower than that of H-β (0.09 mmol g^{-1}). This difference could be related to the larger amount of coordinatively unsaturated Al^{3+} ions, resulting from to the typical crystalline defects of the BEA zeolitic topology, whose proportion is further increased due to its hierarchical porous structure.[49]

In all cases, the incorporation of TiO_2 reduces the BAS concentration, likely due to a partial coverage caused by the metal oxide. Meanwhile, the concentration of LAS increases, which can be directly linked to the presence of TiO_2 nanoparticles. This effect is particularly pronounced in the case of TiO_2/H-β, followed by TiO_2/USY, showing LAS concentrations

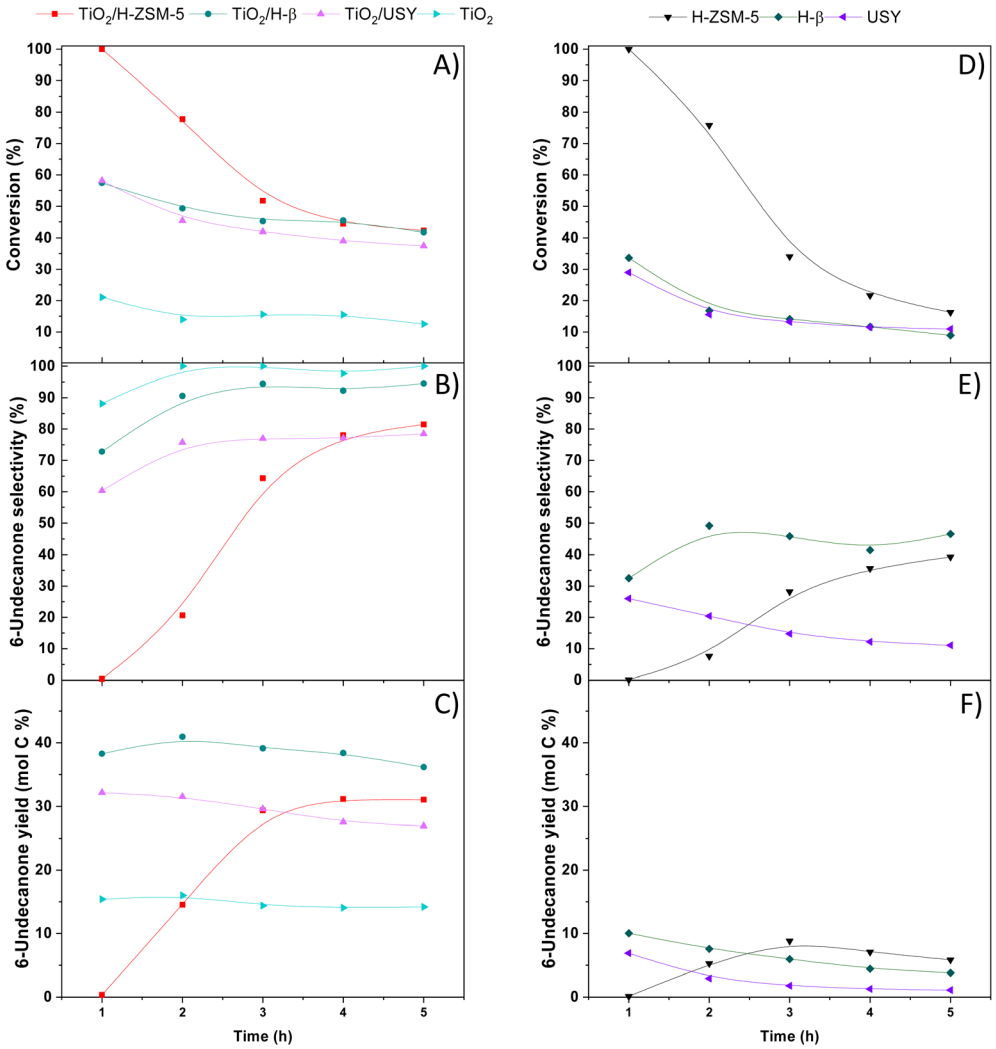

Fig. 2 HA conversion (A and D), 6-UN selectivity (B and E) and 6-UN mol C yield (C and E) over bulk TiO_2, H-ZSM-5, H-β and USY raw supports and TiO_2 supported zeolites.

(0.16 mmol g^{-1} and 0.13 mmol g^{-1}, respectively) higher than that determined for TiO_2/H-ZSM-5 (0.09 mmol g^{-1}).

These TiO_2/zeolite samples were evaluated in the ketonization of HA. Fig. 2 illustrates the evolution of the HA conversion, 6-UN selectivity and mol C yield with the time of stream. The yield of secondary products is provided in the SI (Fig. S9 and S10). For comparison, the catalytic results of the bare zeolites and a commercial bulk TiO_2 (P-25, Thermo Scientific) are also included. The amount of this sample used corresponds to the metal oxide loading deposited on the zeolitic supports.

As discussed in Section 3.1, both H-ZSM-5 and TiO_2/H-ZSM-5 exhibit high HA conversion at short TOS but low selectivity toward the target product due to the conversion of both HA and 6-UN into aromatic hydrocarbons or the occurrence of cracking reactions catalyzed by BAS. However, the progressive deactivation of these acidic sites along the time on stream inhibits these catalytic routes, reducing the HA conversion but increasing both selectivity and yield toward 6-UN.

TiO_2/H-β and TiO_2/USY catalysts show lower conversions at short TOS (1–2 h) compared to TiO_2/H-ZSM-5 (~58–50% *vs.* 100–78%, respectively). However, TiO_2/H-β and TiO_2/USY exhibit a lower deactivation rate, while maintaining more stable conversion values, which can be ascribed to the minor proportion of BAS. Thus, at TOS longer than 3 h, the conversion is stabilized at around 40–45%. For both TiO_2 supported catalysts, the conversion values are almost 30% higher than those attained with the raw supports, which decreases from 35–30% to 14–12%, respectively, due to the deactivation of BAS along the TOS, as observed also for H-ZSM-5 based catalysts.

The selectivity toward 6-UN increases along the time on stream, reaching values in the range of 72.8–94.5% and 60.3–78.4% for TiO_2/H-β and TiO_2/USY, respectively. These results represent a significant improvement over TiO_2/H-ZSM-5 as well as the bare H-β and USY supports. The lower ketone selectivity observed with TiO_2/USY compared to the TiO_2/H-β can be related to the higher formation of cycloalkanes and cracking products, such as propylene.

The carbon yields of 6-UN are presented in Fig. 2C and F. The highest yield is obtained over TiO_2/H-β, which exhibits relatively stable values in the range of 36.1–41.0% mol C along the reaction time, with no aromatic production after 1 h of TOS (Fig. S9). TiO_2/USY achieves lower 6-UN yields ($Y_{6\text{-UN}}$ = 26.9–32.1% mol C) due to the higher production of secondary products such as propylene, cycloalkenes and C_{10} aromatics (Fig. S9 and S10). In the case of TiO_2/H-ZSM-5, the 6-UN yield is initially lower than that of the other two catalysts. However, from a TOS of 3 h onward, it outperforms TiO_2/USY, reaching a ketone yield of 31.5% mol C, once BAS are deactivated. These results confirm that the production of 6-UN strongly depends on the acidic properties of the catalysts, being favored by a high LAS concentration and low contribution of a BAS, as the latter promote secondary reactions such as cyclization, aromatization and cracking reactions. However, the values of the textural parameters, particularly the S_{EXT}, significantly impact on the catalytic performance of the TiO_2 supported zeolites, since the presence of well-developed mesoporosity may enhance the diffusion of the reactant and product molecules, as well as the dispersion of the TiO_2 nanoparticles on the catalyst surface, improving the accessibility of these active sites. Thus, this parameter shows the same tendency as the 6-UN C mol yield: 164 m^2 g^{-1} for TiO_2/H-β ($Y_{6\text{-un}}$ = 41%), 95 m^2 g^{-1} for TiO_2/H-ZSM-5 ($Y_{6\text{-un}}$ = 31.5%) and 59 m^2 g^{-1} for TiO_2/USY ($Y_{6\text{-un}}$ = 27%). These results are further supported by Ti mapping obtained *via* energy-dispersive spectroscopy (EDS) performed on the different TiO_2/zeolites (Fig. S10). As shown, TiO_2/H-β displays a more uniform dispersion of the active phase compared to the other samples. In contrast, TiO_2/H-ZSM-5 exhibits more localised Ti signals, reflecting its relatively lower external surface area and more constrained pore structure. TiO_2/USY exhibits a certain heterogeneity, with the formation of small clusters resulting from the aggregation of TiO_2 particles, which may limit the accessibility to the active sites and reduce its catalytic efficiency.

Interestingly, in all cases, the HA conversion over the TiO_2 supported zeolites is much higher than that of the bulk TiO_2, which ranges from 21.1 to 12.5% along the reaction time. This fact results in a quite lower ketone mol C yield, which remains around 15% along the reaction time, although the 6-UN selectivity is the highest among all the tested catalysts with values comprised between 81.1–100%. Considering that the bulk TiO_2 has a lower S_{BET} (56 m^2 g^{-1}) compared to the TiO_2/zeolites, these results confirm the beneficial role of the textural properties provided by the zeolitic support on the 6-UN production, enhancing the catalytic activity and promoting synergetic effects between the acidic properties of both materials and the higher surface area provided by the zeolitic support.

According to these results, TiO_2/H-β is the best performing catalyst, showing a proper balance between conversion and selectivity, achieving the highest yield of 6-UN, which can be ascribed to its high concentration of LAS and enhanced mesoporous and external surface, leading to an improved dispersion and accessibility of TiO_2 nanoparticles. Despite its large surface area, TiO_2/USY lacks sufficient mesoporous area, leading to lower ketone selectivity and yield. TiO_2/H-ZSM-5 exhibits a high initial HA conversion due to its high BAS concentration, but this also promotes secondary reactions such as aromatization and cracking. However, the progressive BAS deactivation reduces the occurrence of these side reactions and significantly increases ketone production, thus approaching the 6-UN yields obtained over TiO_2/H-β. These results emphasize the importance of optimizing the type of acidic sites in the catalyst as well as the key role of the textural properties of the support in enhancing the catalytic efficiency in ketonization reactions.

3.3 Ketonization of the crude bio-HA over TiO_2/H-β

Following the catalyst screening described in the previous sections, the best performing metal oxide/support combination (TiO_2/H-β) was tested in the ketonization of the bio-HA obtained from the anaerobic fermentation of the ethanol contained in grape pomace residues. The bio-HA was composed by 91.5 wt% of HA, 5.8 wt% of butyric acid (BA), 1.6 wt% of valeric acid (VA) and a 1.1 wt% of water, in addition to minor amounts of other impurities (85 ppm Na^+, 144 ppm K^+, 68 ppm Ca^{2+}, 4 ppm Mg^{2+},

8 ppm Al^{3+}, 1 ppm Fe^{3+}, and 6 ppm Cu^{+}). It should be noted that due to the low concentration of VA in the biogenic substrate, it is not considered in the evaluation of the catalytic results.

First, the ketonization of the bio-HA was carried out at 375 °C to compare the results with those obtained using the pure HA. As observed in Fig. 3A, the HA conversion is quite similar for both substrates (X_{HA} = 55.8–44.6% for the pure HA and X_{HA} = 57.4–41.8% for the biological HA), indicating that, in the presence of a small amount of water and other impurities in the biological HA, the activity of TiO_2/H-β remains quite stable.

The 6-UN selectivity (Fig. 3C) and consequently the 6-UN yield (Fig. 3F) when using the bio-HA ($S_{6\text{-UN}}$ = 87.8%) are somewhat lower than when using the pure HA ($S_{6\text{-UN}}$ = 94.5%). This decrease is attributed to the occurrence of cross-ketonization reactions of HA with BA to produce 4-nonanone (4-NO), which can also be further used as jet fuel precursor. The

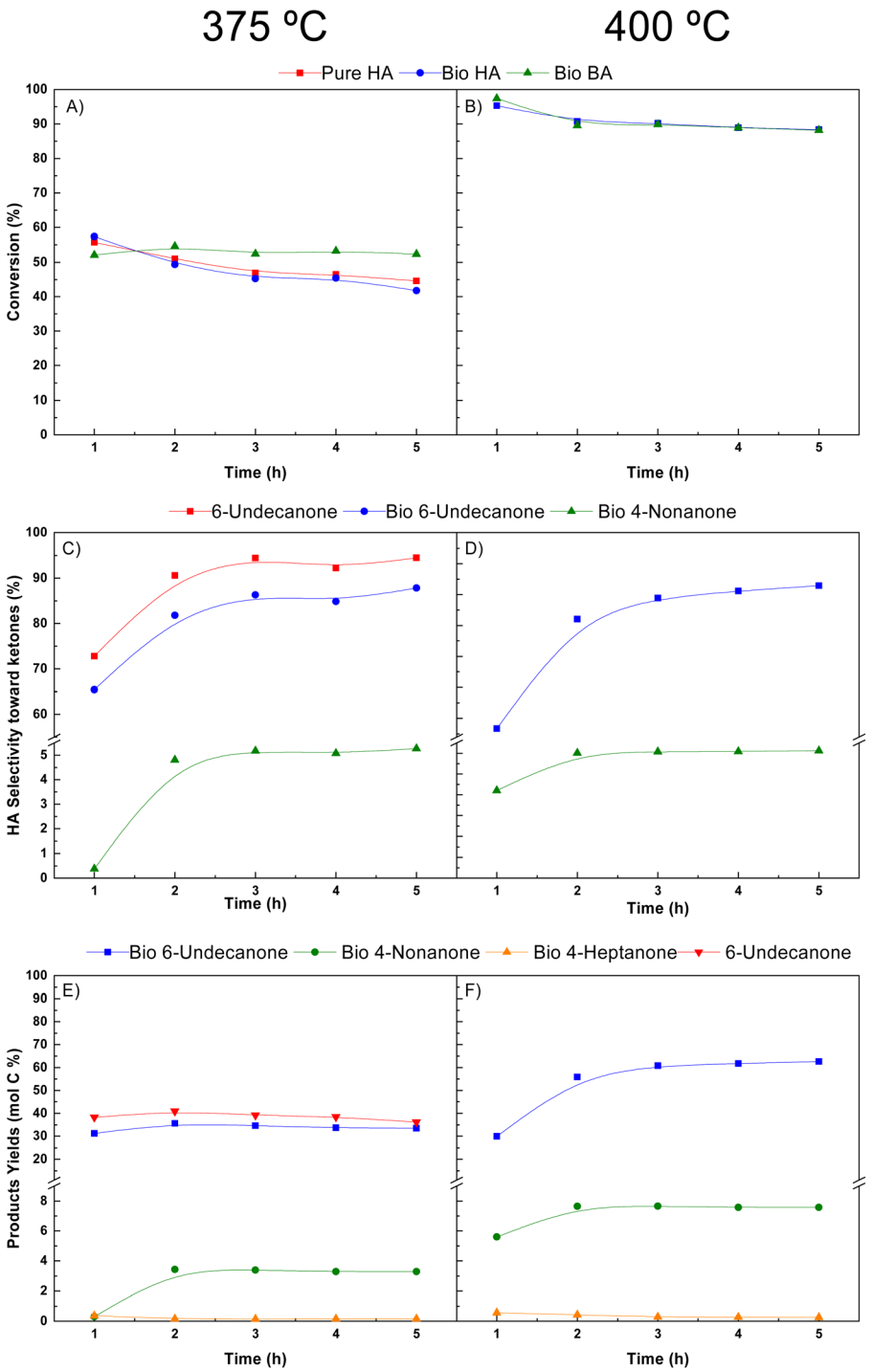

Fig. 3 Conversion of carboxylic acids using a real HA substrate at 375 °C (A) and 400 °C (B); selectivity of HA toward the formation of ketones at 375 °C (C) and 400 °C (D); and ketone mol C yields at 375 °C (E) and 400 °C (F).

formation of 4-nonanone is favored over the production of 6-unecanone because the rate of cross-ketonization at twice the rate of homo-ketonization.[50] In addition, shorter-chain carboxylic acids are more reactive than those with longer carbon chains.[19] In this sense, in cross-ketonization reactions, one carboxylic acid provides an acyl group, while the other supplies an alkyl group. Alkyl groups are more easily formed from shorter-chain carboxylic acids because they are more susceptible to deoxygenation. As a result, shorter-chain acids facilitate the formation of alkyl groups, which then react with acyl groups from longer-chain acids, promoting cross-ketonization.[51,52] In addition, the presence of alkali metals (Na^+ or K^+) in biogenic feedstock may also have contributed to the lower selectivity toward 6-undecanone. These metals are known to increase surface basicity and promote the formation of oxygen vacancies. Such effects enhance cross-ketonization reactions, particularly between acids of different chain lengths, as observed between HA and BA. Furthermore, alkali cations can stabilize enolate intermediates, improving catalyst lifetime by suppressing coke formation.[53,54]

To optimize the conversion of the bio-HA, an additional test was performed at 400 °C (Fig. 3B, D and E). As observed, the temperature increase has a positive impact on all VFAs conversions, achieving values of 95.3–88.4% for HA and 97.4–88.2% for BA.

At 400 °C, the selectivity toward ketones decreases, especially at 1 h of TOS ($S_{6\text{-UN}} = 72.8\%$ at 375 °C *vs.* $S_{6\text{-UN}} = 36.7\%$ at 400 °C), due to the production of aromatic hydrocarbons (Fig. S12). Following the trend observed in previous experiments, the aromatic production decreases along the time on stream as the BAS of the support are deactivated, leading to an increase in the overall ketone selectivity. Specifically, the 6-UN selectivity is slightly lower at 400 °C ($S_{6\text{-UN}} = 82.9\%$ at TOS = 5 h) than that at 375 °C ($S_{6\text{-UN}} = 87.8\%$ at TOS = 5 h) which can be related to the higher selectivity to 4-nonanone ($S_{4\text{-NO}} = 5.3\%$ at 375 °C *vs.* $S_{4\text{-NO}} = 6.1\%$ at 400 °C at TOS = 5 h) as well as the higher formation of gaseous products (Fig. S12). The selectivity of BA toward 4-nonanone is higher than that toward 4-heptanone, its homo-ketonization product, which can be attributed to the higher rate of cross-ketonization compared to homo-ketonization, which can be also favored by the much higher proportion of HA in the reaction medium ($S_{4\text{-NO}} = 53.8\%$ *vs.* $S_{4\text{-HE}} = 6.3\%$ at a TOS of 5 h) and 400 °C ($S_{4\text{-NO}} = 73.6\%$ *vs.* $S_{4\text{-HE}} = 6.1\%$ at a TOS of 5 h) (Fig. S13).

All these results denote that the use of a biotechnological derived HA, containing impurities and other carboxylic acids, does not significantly affect the activity of TiO_2/H-β catalyst in comparison with pure HA. Thus, similar amounts of 6-UN are produced from the homo-ketonization of HA but also yielding other products of interest when using the real substrate, such as 4-nonanone from the cross-ketonization of HA with BA.

Finally, the stability and deactivation of the TiO_2/H-β catalyst have been studied by performing an experiment of 18 h using the bio-HA substrate at a temperature of 400 °C. The VFAs conversion as well as the selectivity and yields toward 6-undecanone and 4-nonanone are presented in Fig. 4.

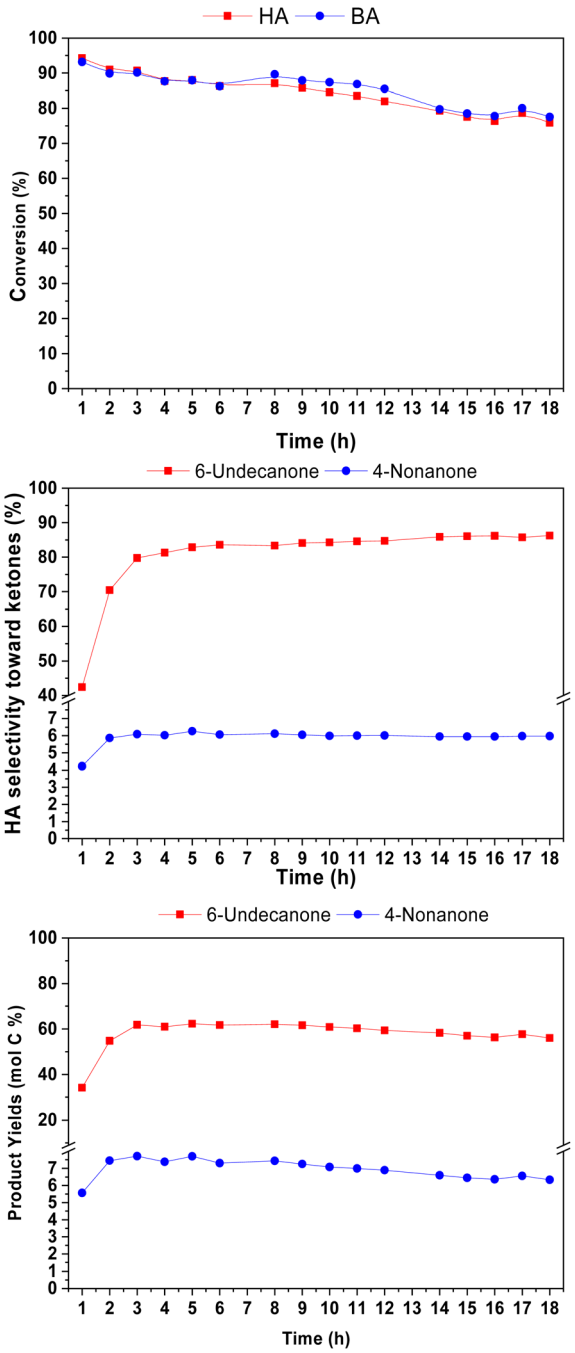

Fig. 4 Conversion of carboxylic acids using a real HA substrate (A); selectivity of HA toward the formation of ketones (B); and ketone mol C yields (C) at 400 °C during 18 h of TOS.

The VFAs conversion with the biogenic substrate varies along with the TOS, following a similar trend as observed in the previous experiments (Fig. 4A). First, the conversion of carboxylic acids is very high at short of TOS, ($X_{HA} = 94.3\%$; $X_{BA} = 93.2\%$), which decreases slightly at a TOS of 3 h due to the deactivation of BAS. This behavior is consistent with the observed simultaneous reduction in gases (Fig. S14) as well as aromatic and cyclic hydrocarbon yields and the progressive increase in ketones production. After that this time, the VFAs

conversion remains quite stable, reaching values of 83.5% for HA and 86–87% for BA, respectively, while the selectivity toward 6-UN and 4-NO remains almost constant until the end of the experiment. As a result, the mol C yield varies from 61.8 to 56.0 mol C % for 6-UN and from 7.8 to 6.3 mol C % for 4-NO at the end of the experiment, indicating that the activity of the LAS present in the zeolite and those provided by TiO_2 is largely preserved.

3.4 Effect of zeolite BAS elimination on the performance of the TiO_2/H-ZSM-5 catalyst

As shown in the previous section, acidity greatly influences the ketonization of HA over TiO_2 zeolitic supported catalysts. A high BAS concentration promotes the occurrence of secondary reactions, such as cracking and aromatization, thereby reducing the ketone production. According to the literature, the BAS acidity of zeolites can be modulated by Na-ion exchange treatments, which could enhance the ketonization activity of the TiO_2-supported zeolites. To evaluate this hypothesis and considering the high concentration of BAS in ZSM-5 zeolite, this support was subjected to a Na-ion exchange treatment, using sodium carbonate as the Na source. In addition, to determine the role of the LAS of the raw zeolite, a TiO_2/silicalite (with $[Si/Al]_{MOL} = \infty$) was also evaluated in this section. The synthesis of this zeolitic support has been reported elsewhere,[55] while the TiO_2 deposition was carried out as previously described.

Wide angle XRD analyses (shown in Fig. S15) indicate that the ion exchange process does not have a significant effect on the crystallinity of H-ZSM-5 zeolite, as the characteristic reflections of the MFI structure are seen, but with lower signal intensity. The S_{BET} decreased from 388 $m^2\ g^{-1}$ to 358 $m^2\ g^{-1}$ after the exchange process, due to the slight reduction observed in the S_{EXT} (from 106 to 81 $m^2\ g^{-1}$). However, the textural parameters related to the zeolitic micropores are quite similar, denoting that the Na-exchange treatment does not have a significant impact on the zeolitic structure. As in the case of the previous catalysts, the presence of TiO_2 nanoparticles on the catalyst surface is evidenced by the signals of the TiO_2 anatase phase observed in the XRD patterns, which leads to a certain reduction in the textural parameters. However, the greater modification of the Na-ion exchange occurs in the acidic properties (Table 3). Thus, the concentration of BAS is almost null, while the concentration of LAS increases from 0.03 to 0.22 mmol g^{-1} due to the introduction of Na+ ions. After TiO_2 incorporation, LAS concentration increases slightly (0.25 mmol g^{-1}), and a small amount of BAS is generated (0.04 mmol g^{-1}).

The catalytic behavior of these samples is compared in Fig. 5. Na/ZSM-5 zeolite exhibits poor catalytic performance, with HA conversions around 10% and 6-UN selectivity close to 15%

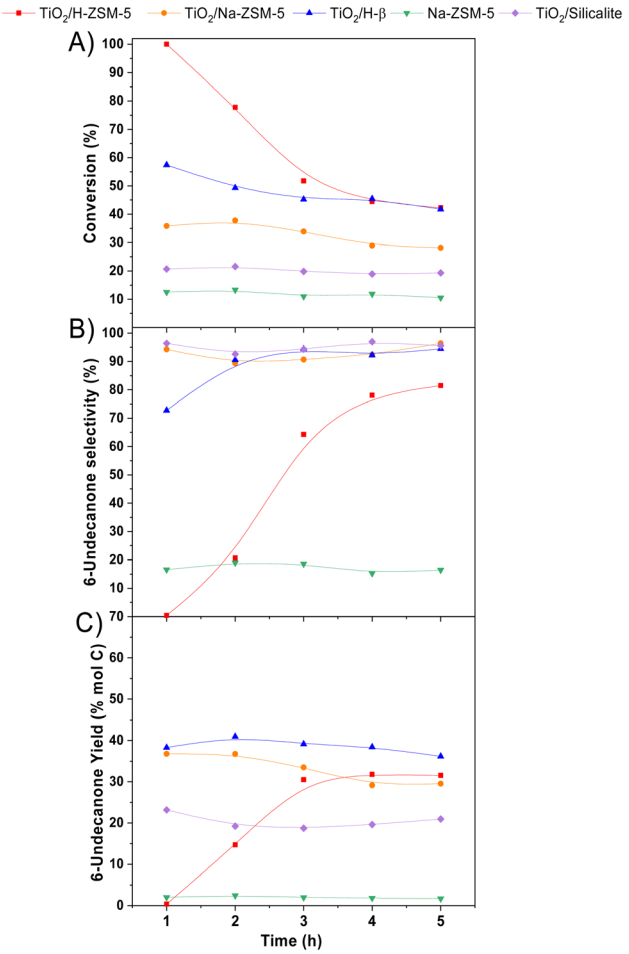

Fig. 5 HA conversion (A), 6-UN selectivity (B) and 6-UN mol C yield (C), reached on the HA ketonization reactions over TiO_2/H-ZSM-5, Na-ZSM-5, TiO_2/Na-ZSM-5, TiO_2/H-β and TiO_2/silicalite.

Table 3 Physical and chemical characterization of H-ZSM-5, Na-ZSM-5, TiO_2/H-ZSM-5, TiO_2/Na-ZSM-5 and TiO_2/silicalite

Catalysts	S_{BET}[a] ($m^2\ g^{-1}$)	S_{MZ}[b] ($m^2\ g^{-1}$)	S_{MS+EXT}[b] ($m^2\ g^{-1}$)	V_{MZ}[b] ($cm^3\ g^{-1}$)	V_T[c] ($cm^3\ g^{-1}$)	C_L[d] (mmol g^{-1})	C_B[d] (mmol g^{-1})	Metal oxide loading[e] (wt%)
H-ZSM-5	388	282	106	0.176	0.458	0.03	0.25	—
Na-ZSM-5	358	277	81	0.173	0.529	0.22	0.00	—
TiO_2/H-ZSM-5	337	242	95	0.151	0.417	0.09	0.19	16.8
TiO_2/Na-ZSM-5	321	237	84	0.147	0.435	0.25	0.04	16.5
TiO_2/silicalite	363	304	59	0.189	0.283	0.05	0.01	16.4

[a] BET surface area from Ar adsorption–desorption isotherms (−186 °C). [b] Calculated by applying NL-DFT method to Ar adsorption–desorption isotherms (−186 °C). [c] Measured at $P/P_0 = 0.97$. [d] Determined by means of pyridine adsorption followed by FT-IR. [e] Estimated from ICP-AOS analyses.

along the TOS, indicating that the Lewis acid sites introduced by sodium ions are ineffective for catalyzing HA ketonization. In contrast, the incorporation of TiO_2 over Na-ZSM-5 significantly enhances the catalytic activity, increasing the HA conversion and 6-UN selectivity to the range of 30–35% and 89–96.4%, respectively, along the reaction time, highlighting the catalytic effect on the TiO_2 nanoparticles. Nevertheless, the conversion achieved with TiO_2/Na-ZSM-5 is still significantly lower than that obtained with TiO_2/H-ZSM-5, which shows values decreasing from 98% to 45% along the TOS. Notably, when BAS are deactivated in TiO_2/H-ZSM-5, the conversion drops, but the 6-UN selectivity increases, resulting in similar mol C yields of 6-UN (Fig. 5C).

The role of the LAS of the zeolitic support is further confirmed by the catalytic results obtained over TiO_2/silicalite, which presents only the LAS provided by TiO_2. Although this sample exhibits an excellent selectivity toward 6-UN, the HA conversion remains around 20% along the TOS, leading to significantly lower ketone yields compared to ZSM-5 based catalysts. Nevertheless, the selectivity and yield toward 6-UN of these samples are still lower compared to TiO_2/H-β, suggesting that not only acidic and but also textural properties and TiO_2 dispersion play a key role in determining the production of 6-UN.

4. Conclusions

This work investigates the ketonization of hexanoic acid (HA) to obtain 6-undecanone (6-UN) over bifunctional catalysts comprising metal oxides (TiO_2, ZrO_2, CeO_2) supported on different zeolitic supports. The metal oxide phases screening performed using a commercial H-ZSM-5 as a support denoted the ketone production was catalyzed by LAS, while the presence of BAS promoted the occurrence of side reactions producing gaseous olefins and aromatic hydrocarbons. BAS suffered a rapid deactivation along the TOS, reducing the HA conversion but improving the selectivity and mol C yield toward 6-UN. Among the oxides tested, TiO_2 exhibited the highest ketonization activity and 6-undecanone yield.

Then, the catalytic behavior of TiO_2 supported on H-ZSM-5, H-β and USY zeolites was also evaluated. TiO_2/H-β and TiO_2/USY exhibited lower formation of cracking and aromatization products and slower deactivation rates compared to TiO_2/H-ZSM-5, due to their lower BAS content. Consequently, the 6-UN yield remained more stable over time. TiO_2/H-β was the best-performing catalyst, reaching a 6-UN mol C yield of 41.0% after 5 hours of TOS. This outstanding performance was attributed to its high LAS concentration and its significant mesoporous and external surface area, which enhanced mass transfer and TiO_2 dispersion. This catalyst maintained this excellent activity when applied to the ketonization of a crude biogenic HA (91.5% pure) obtained from the anaerobic fermentation of the ethanol contained in grape pomace. Notably, after 18 hours of reaction, the selectivity toward both homo- and cross-ketonization products remained remarkably stable, and only a slight decrease in HA was observed, demonstrating the robustness of this catalytic system using a real fermentative substrate.

Finally, the H-ZSM-5 was subjected to a Na-ion exchange treatment to eliminate BAS. As a result, when TiO_2 was incorporated, the catalyst showed a more stable 6-UN production, avoiding the formation of cracking and aromatization products. Interestingly, this catalyst outperformed TiO_2/silicalite, highlighting the beneficial role of LAS provided by the zeolitic support in enhancing ketonization activity of these zeolites. Nevertheless, both HA conversion and ketone yield were not as good as those obtained over the TiO_2/H-β ($Y_{6\text{-un}} = 29.5\%$ mol C over TiO_2/Na-ZSM-5 *vs.* $Y_{6\text{-un}} = 41.0\%$ mol C over the TiO_2/H-β), evidencing that not only the acidic properties had a great impact on the ketonization of HA, but also the textural properties played a significant influence in this process.

Author contributions

Adrián Lago: investigation, data curation, formal analysis, writing – original draft. Lorenzo Bertin: resources, writing review and editing. Gonzalo A. Martinez: resources, writing review and editing. Emma Jones: resources, writing review and editing. Jacopo De Maron: conceptualization, methodology, writing review and editing. Tommaso Tabanelli: conceptualization, writing review and editing, supervision. Fabrizio Cavani: writing review and editing, supervision. Cristina González-Fernández: conceptualization, writing review and editing. David P. Serrano: writing review and editing, supervision. Inés Moreno: conceptualization, writing – original draft, writing review and editing, supervision.

Conflicts of interest

The authors declare that they have no competing interests.

Data availability

All datasets are available from the corresponding author upon reasonable request.

The SI file contains XRD characterization data, Ar physisorption isotherms, TEM and SEM images (with corresponding elemental mapping) of TiO_2 supported on H-ZSM-5, H-USY, and H-β, as well as the secondary product distribution in the gas and liquid phases from the HA and bio-HA ketonization tests. See DOI: **https://doi.org/10.1039/d5se00930h**.

Acknowledgements

Adrián Lago acknowledge that this work was supported by the grant PRE2020-094485 funded by MCIN/AEI/10.13039/501100011033 and by "ESF Investing in your future." Tomasso Tabanelli and Jacopo De Maron acknowledge funding from European Commission, NextGenerationEU – Piano Nazionale di Ripresa e Resilienza (PNRR) – Ministero dell'Università e della Ricerca (MUR); (project number PE_00000021). Fabrizio Cavani and Lorenzo Bertin acknowledge the MICS (Made in Italy – Circular and Sustainable) Extended Partnership and received funding from the European Union Next-GenerationEU (PIANO NAZIONALE DI RIPRESA E RESILIENZA (PNRR) – MISSIONE 4

COMPONENTE 2, INVESTIMENTO 1.3 – D. D. 1551.11-10-2022, PE00000004).

References

1 European Union Aviation Safety Agency, European Aviation Environmental Report 2022, 2022.
2 European Commission, Reducing emissions from aviation. https://climate.ec.europa.eu/eu-action/transport/reducing-emissions-aviation_en, accessed 2025-01-10.
3 European Union, Regulation (EU) 2023/2405 of the European Parliament and of the Council of 18 October 2023 on Ensuring a Level Playing Field for Sustainable Air Transport (ReFuelEU Aviation), *Off. J. Eur. Union, L*, 2023, **L**, 1–30.
4 K. Soubly, L. U. Calderwood, C. Wolff, F. Delasalle, L. Pinnell, C. E. Agnes and W. E. Forum, Guidelines for a Sustainable Aviation Fuel Blending Mandate in Europe, 2021, https://www.weforum.org/reports/guidelines-for-a-sustainable-aviation-fuel-blending-mandate-in-europe/.
5 N. A. Huq, G. R. Hafenstine, X. Huo, H. Nguyen, S. M. Tifft, D. R. Conklin, D. Stück, J. Stunkel, Z. Yang, J. S. Heyne, M. R. Wiatrowski, Y. Zhang, L. Tao, J. Zhu, C. S. McEnally, E. D. Christensen, C. Hays, K. M. van Allsburg, K. A. Unocic, H. M. Meyer, Z. Abdullah and D. R. Vardon, Toward Net-Zero Sustainable Aviation Fuel with Wet Waste–derived Volatile Fatty Acids, *Proc. Natl. Acad. Sci. U. S. A.*, 2021, **118**(13), e2023008118, DOI: 10.1073/pnas.2023008118.
6 O. Rosales Calderon, L. Tao, Z. Abdullah, M. Talmadge, A. Milbrandt, S. Smolinski, K. Moriarty, A. Bhatt, Y. Zhang, V. Ravi, C. Skangos, R. Davis and C. Payne, *Sustainable Aviation Fuel State-of-Industry Report: Hydroprocessed Esters and Fatty Acids Pathway*, National Renewable Energy Laboratory, Golden, CO, 2024, NREL/TP-5400-87803, Available at: https://www.nrel.gov/docs/fy24osti/87803.pdf.
7 Fuels, L. G.No Title. https://www.lighthousegreenfuels.co.uk/the-future-of-sustainable-aviation-fuel-exploring-key-production-pathways/accessed 2024-10-22.
8 S. van Dyk and J. Saddler, Progress in Commercialization of Biojet/Sustainable Aviation Fuels (SAF): Technologies and Policies, IEA Bioenergy: Task 39, 2024.
9 A. Gagliardi, G. Balestra, J. De Maron, R. Mazzoni, T. Tabanelli and F. Cavani, Ethanol to Gasoline and Sustainable Aviation Fuel Precursors: An Innovative Cascade Strategy over Zr-Based Multifunctional Catalysts in the Gas Phase, *Appl. Catal., B*, 2024, **349**, 123865, DOI: 10.1016/j.apcatb.2024.123865.
10 J. X. Lim, Y. Zhou and V. M. Vadivelu, Enhanced Volatile Fatty Acid Production and Microbial Population Analysis in Anaerobic Treatment of High Strength Wastewater, *J. Water Process Eng.*, 2020, **33**, 101058, DOI: 10.1016/j.jwpe.2019.101058.
11 S. Harirchi, S. Wainaina, T. Sar, S. A. Nojoumi, M. Parchami, M. Parchami, S. Varjani, S. K. Khanal, J. Wong, M. K. Awasthi and M. J. Taherzadeh, Microbiological Insights into Anaerobic Digestion for Biogas, Hydrogen or Volatile Fatty Acids (VFAs): A Review, *Bioengineered*, 2022, **13**(3), 6521–6557, DOI: 10.1080/21655979.2022.2035986.
12 J. H. Miller, G. R. Hafenstine, H. H. Nguyen and D. R. Vardon, Kinetics and Reactor Design Principles of Volatile Fatty Acid Ketonization for Sustainable Aviation Fuel Production, *Ind. Eng. Chem. Res.*, 2022, **61**(8), 2997–3010, DOI: 10.1021/acs.iecr.1c04548.
13 X. Li, L. Zhang, S. Wang and Y. Wu, Recent Advances in Aqueous-Phase Catalytic Conversions of Biomass Platform Chemicals Over Heterogeneous Catalysts, *Front. Chem.*, 2020, **7**, 1–21, DOI: 10.3389/fchem.2019.00948.
14 S. Zhang, B. Jiang, Y. Yang, Z. Liao, Z. Huang, J. Sun, J. Wang and Y. Yang, Hydrophobic Copper Doped Ceria-Based Catalyst for Ketonization of Acetic Acid by Suppressing Water Inhibition, *Appl. Surf. Sci.*, 2024, **652**, 159371, DOI: 10.1016/j.apsusc.2024.159371.
15 Y. Guo, Y. Qin, H. Liu, H. Wang, J. Han, X. Zhu and Q. Ge, CeO2 Facet-Dependent Surface Reactive Intermediates and Activity during Ketonization of Propionic Acid, *ACS Catal.*, 2022, **12**(5), 2998–3012, DOI: 10.1021/acscatal.1c05994.
16 Z. Yang, Q. Yu, H. Wang, Q. Ge and X. Zhu, Ketonization of Propionic Acid over TS-1 and Ti-Beta Zeolites: Mechanism and Effects of Topology and Hydrophobicity, *J. Catal.*, 2024, **429**, 115247, DOI: 10.1016/j.jcat.2023.115247.
17 J. De Maron, L. Bellotti, A. Baldelli, A. Fasolini, N. Schiaroli, C. Lucarelli, F. Cavani and T. Tabanelli, Evaluation of the Catalytic Activity of Metal Phosphates and Related Oxides in the Ketonization of Propionic Acid, *Sustainable Chem.*, 2022, **3**(1), 58–75, DOI: 10.3390/suschem3010005.
18 J. Cao, S. Ding, H. Wang, J. Han, Q. Ge and X. Zhu, Conversion of C2-4 Carboxylic Acids to Hydrocarbons on HZSM-5: Effect of Carbon Chain Length, *Ind. Eng. Chem. Res.*, 2019, 2–11, DOI: 10.1021/acs.iecr.9b01755.
19 O. Nagashima, S. Sato, R. Takahashi and T. Sodesawa, Ketonization of Carboxylic Acids over CeO2-Based Composite Oxides, *J. Mol. Catal. A: Chem.*, 2005, **227**(1–2), 231–239, DOI: 10.1016/j.molcata.2004.10.042.
20 G. A. Martinez, S. Puccio, J. M. B. Domingos, E. Morselli, C. Gioia, P. Marchese, A. M. Raspolli Galletti, A. Celli, F. Fava and L. Bertin, Upgrading Grape Pomace Contained Ethanol into Hexanoic Acid, Fuel Additives and a Sticky Polyhydroxyalkanoate: An Effective Alternative to Ethanol Distillation, *Green Chem.*, 2022, **24**(7), 2882–2892, DOI: 10.1039/d2gc00044j.
21 S. Frigo, A. M. Raspolli Galletti, S. Fulignati, D. Licursi, L. Bertin, G. A. Martinez and G. Pasini, Synthesis of 1-Hexanol/Hexyl Hexanoate Mixtures from Grape Pomace: Insights on Diesel Engine Performances at High Bio-Blendstock Loadings, *Energies*, 2023, **16**(19), 6789, DOI: 10.3390/en16196789.
22 V. D'Ambrosio, G. Martinez, E. Jones, L. Bertin and C. Pastore, Ethyl Hexanoate Rich Stream from Grape Pomace: A Viable Route to Obtain Fine Chemicals from Agro by-Products, *Sep. Purif. Technol.*, 2023, **309**, 123100, DOI: 10.1016/j.seppur.2023.123100.
23 E. V. Fufachev, B. M. Weckhuysen and P. C. A. Bruijnincx, Tandem Catalytic Aromatization of Volatile Fatty Acids,

Green Chem., 2020, **22**(10), 3229–3238, DOI: 10.1039/D0GC00964D.

24 F. Lin, W. Hu, N. R. Jaegers, F. Gao, J. Z. Hu, H. Wang and Y. Wang, Elucidation of the Roles of Water on the Reactivity of Surface Intermediates in Carboxylic Acid Ketonization on TiO2, *J. Am. Chem. Soc.*, 2023, **145**(1), 99–109, DOI: 10.1021/jacs.2c08511.

25 J. De Maron, D. Cesari, S. Banu Rameesdeen, T. Tabanelli, A. Fasolini, F. Basile and F. Cavani, An Innovative Catalytic Pathway for the Synthesis of Acyl Furans: The Cross-Ketonization of Methyl 2-Furoate with Carboxylic Acids, *Green Chem.*, 2023, **25**(18), 7381–7392, DOI: 10.1039/D3GC01992F.

26 J. De Maron, A. Safarova, C. Ursu, G. M. D'Onofrio, E. T. Brandi, A. Fasolini, G. Gottardi, F. Basile, F. Cavani and T. Tabanelli, Promoting Zirconia with Carbon: Enhanced Hybrid ZrO2/C Catalyst for the Ketonization of Diluted Aqueous Acetic Acid, *Carbon*, 2025, **238**, 120203, DOI: 10.1016/j.carbon.2025.120203.

27 Y. Guo, Q. Yu, H. Fang, H. Wang, J. Han, Q. Ge and X. Zhu, Ce-UiO-66 Derived CeO2 Octahedron Catalysts for Efficient Ketonization of Propionic Acid, *Ind. Eng. Chem. Res.*, 2020, **59**(39), 17269–17278, DOI: 10.1021/acs.iecr.0c01238.

28 T. N. Pham, T. Sooknoi, S. P. Crossley and D. E. Resasco, Ketonization of Carboxylic Acids: Mechanisms, Catalysts, and Implications for Biomass Conversion, *ACS Catal.*, 2013, **3**(11), 2456–2473, DOI: 10.1021/cs400501h.

29 L. M. Orozco, M. Renz and A. Corma, Cerium Oxide as a Catalyst for the Ketonization of Aldehydes: Mechanistic Insights and a Convenient Way to Alkanes without the Consumption of External Hydrogen, *Green Chem.*, 2017, **19**(6), 1555–1569, DOI: 10.1039/c6gc03511f.

30 E. V. Fufachev, B. M. Weckhuysen and P. C. A. Bruijnincx, Crystal Phase Effects on the Gas-Phase Ketonization of Small Carboxylic Acids over TiO2 Catalysts, *ChemSusChem*, 2021, **14**(13), 2710–2720, DOI: 10.1002/cssc.202100721.

31 Y. Lee, J. W. Choi, D. J. Suh, J. M. Ha and C. H. Lee, Ketonization of Hexanoic Acid to Diesel-Blendable 6-Undecanone on the Stable Zirconia Aerogel Catalyst, *Appl. Catal., A*, 2015, **506**, 288–293, DOI: 10.1016/j.apcata.2015.09.008.

32 B. Boekaerts and B. F. Sels, Catalytic Advancements in Carboxylic Acid Ketonization and Its Perspectives on Biomass Valorisation, *Appl. Catal., B*, 2021, **283**, 119607, DOI: 10.1016/j.apcatb.2020.119607.

33 X. Wang, S. Ding, H. Wang, X. Liu, J. Han, Q. Ge and X. Zhu, Conversion of Propionic Acid and 3-Pentanone to Hydrocarbons on ZSM-5 Catalysts: Reaction Pathway and Active Site, *Appl. Catal., A*, 2017, **545**, 79–89, DOI: 10.1016/j.apcata.2017.07.037.

34 S. Shao, X. Xia, X. Li, H. Zhang and R. Xiao, Aldol Condensation of Biomass-Derived Aldehydes and Ketones Followed by Hydrogenation over Ni/HZSM-5 to Produce Aviation Fuel: Role of Acid Sites, *Fuel Process. Technol.*, 2023, **250**, 107904, DOI: 10.1016/j.fuproc.2023.107904.

35 Q. Yu, Y. Guo, X. Wu, Z. Yang, H. Wang, Q. Ge and X. Zhu, Ketonization of Propionic Acid on Lewis Acidic Zr-Beta Zeolite with Improved Stability and Selectivity, *ACS Sustain. Chem. Eng.*, 2021, **9**(23), 7982–7992, DOI: 10.1021/acssuschemeng.1c02290.

36 W. Yin, Z. Yang, Z. Liu, C. Liu, Q. Ge and X. Zhu, Selective Ketonization of Propionic Acid on Fe-MFI Zeolites: The Crucial Role of Acid Strength and Density, *Catal. Sci. Technol.*, 2025, 1–152, DOI: 10.1039/D5CY00175G.

37 H. Hernando, B. Puértolas, P. Pizarro, J. Fermoso, J. Pérez-Ramírez and D. P. Serrano, Cascade Deoxygenation Process Integrating Acid and Base Catalysts for the Efficient Production of Second-Generation Biofuels, *ACS Sustain. Chem. Eng.*, 2019, **7**(21), 18027–18037, DOI: 10.1021/acssuschemeng.9b04921.

38 H. Hernando, A. M. Hernández-Giménez, C. Ochoa-Hernández, P. C. A. Bruijnincx, K. Houben, M. Baldus, P. Pizarro, J. M. Coronado, J. Fermoso, J. Čejka, B. M. Weckhuysen and D. P. Serrano, Engineering the Acidity and Accessibility of the Zeolite ZSM-5 for Efficient Bio-Oil Upgrading in Catalytic Pyrolysis of Lignocellulose, *Green Chem.*, 2018, **20**(15), 3499–3511.

39 M. Álvarez, J. Cueto, D. P. Serrano, P. Marín and S. Ordóñez, Influence of the Synthesis Method of Cu/Y Zeolite Catalysts for the Gas Phase Oxidative Carbonylation of Methanol to Dimethyl Carbonate, *Catal. Today*, 2024, **428**, 114464, DOI: 10.1016/j.cattod.2023.114464.

40 M. d. M. Alonso-Doncel, E. A. Giner, D. de la Calle, J. Cueto, P. Horcajada, R. A. García-Muñoz and D. P. Serrano, Synthesis of Dendritic ZSM-5 Zeolite through Micellar Templating Controlled by the Amphiphilic Organosilane Chain Length, *Cryst. Growth Des.*, 2023, **23**(8), 5658–5670, DOI: 10.1021/acs.cgd.3c00326.

41 D. P. Serrano, J. Aguado and Á. Peral, Controlling the Generation of Hierarchical Porosity in ZSM-5 by Changing the Silanization Degree of Protozeolitic Units, in *Studies in Surface Science and Catalysis*, 2008, pp. 123–128, DOI: 10.1016/S0167-2991(08)80162-0.

42 J. Fermoso, H. Hernando, P. Jana, I. Moreno, J. Přech, C. Ochoa-Hernández, P. Pizarro, J. M. Coronado, J. Čejka and D. P. Serrano, Lamellar and Pillared ZSM-5 Zeolites Modified with MgO and ZnO for Catalytic Fast-Pyrolysis of Eucalyptus Woodchips, *Catal. Today*, 2016, **277**, 171–181.

43 S. Gutiérrez-Rubio, A. Berenguer, J. Přech, M. Opanasenko, C. Ochoa-Hernández, P. Pizarro, J. Čejka, D. P. Serrano, J. M. Coronado and I. Moreno, Guaiacol Hydrodeoxygenation over Ni2P Supported on 2D-Zeolites, *Catal. Today*, 2019, **345**, 45–58, DOI: 10.1016/j.cattod.2019.11.015.

44 P. Reif, N. K. Gupta and M. Rose, Liquid Phase Aromatization of Bio-Based Ketones over a Stable Solid Acid Catalyst under Batch and Continuous Flow Conditions, *Catal. Commun.*, 2022, **163**, 106402, DOI: 10.1016/j.catcom.2022.106402.

45 S. Ding, H. Wang, J. Han, X. Zhu and Q. Ge, Ketonization of Propionic Acid to 3-Pentanone over Ce X Zr 1- X O 2 Catalysts: The Importance of Acid-Base Balance, *Ind. Eng. Chem. Res.*, 2018, **57**(50), 17086–17096, DOI: 10.1021/acs.iecr.8b04208.

46 J. Fuhse and F. Bandermann, Conversion of Organic Oxygen Compounds and Their Mixtures on H-ZSM-5, *Chem. Eng. Technol.*, 1987, **10**(1), 323–329, DOI: **10.1002/ceat.270100139**.
47 J. H. Miller, M. Al Abri, J. Stunkel, A. J. Koehler, M. R. Wiatrowski, R. L. McCormick, G. Fioroni, J. Luecke, C. Paeper and M. Arellano-Treviño, Catalytic Upgrading of Wet Waste-Derived Carboxylic Acids to Sustainable Aviation Fuel and Chemical Feedstocks, *EES Catal.*, 2024, **2**(5), 1111–1125, DOI: **10.1039/d4ey00087k**.
48 M. M. J. Treacy and J. B. Higgins, *Collection of Simulated XRD Powder Patterns for Zeolites*, Elsevier Science, 5th edn, 2007.
49 S. Prodinger, H. Shi, H. Wang, M. A. Derewinski and J. A. Lercher, Impact of Structural Defects and Hydronium Ion Concentration on the Stability of Zeolite BEA in Aqueous Phase, *Appl. Catal., B*, 2018, **237**, 996–1002, DOI: **10.1016/j.apcatb.2018.06.065**.
50 C. A. Gaertner, J. C. Serrano-Ruiz, D. J. Braden and J. A. Dumesic, Ketonization Reactions of Carboxylic Acids and Esters over Ceria-Zirconia as Biomass-Upgrading Processes, *Ind. Eng. Chem. Res.*, 2010, **49**(13), 6027–6033, DOI: **10.1021/ie1004338**.
51 A. V. Ignatchenko, J. S. Deraddo, V. J. Marino and A. Mercado, Cross-Selectivity in the Catalytic Ketonization of Carboxylic Acids, *Appl. Catal., A*, 2015, **498**, 10–24, DOI: **10.1016/j.apcata.2015.03.017**.
52 A. V. Ignatchenko and E. I. Kozliak, Distinguishing Enolic and Carbonyl Components in the Mechanism of Carboxylic Acid Ketonization on Monoclinic Zirconia, *ACS Catal.*, 2012, **2**(8), 1555–1562, DOI: **10.1021/cs3002989**.
53 A. V. Ignatchenko, Multiscale Approach for the Optimization of Ketones Production from Carboxylic Acids by the Decarboxylative Ketonization Reaction, *Catal. Today*, 2019, **338**, 3–17, DOI: **10.1016/j.cattod.2019.06.080**.
54 K. Parida and H. K. Mishra, Catalytic Ketonisation of Acetic Acid over Modified Zirconia, *J. Mol. Catal. A: Chem.*, 1999, **139**(1), 73–80, DOI: **10.1016/S1381-1169(98)00184-8**.
55 D. P. Serrano, J. A. Botas, P. Pizarro, I. Moreno and G. Gómez, Hydrogen Production through Catalytic Methane Decomposition Promoted by Pure Silica Materials, *Int. J. Hydrogen Energy*, 2015, **40**(15), 5237–5243, DOI: **10.1016/j.ijhydene.2015.01.056**.